A Highly Efficient Composite Catalyst Constructed From NH_2-MIL-125(Ti) and Reduced Graphene Oxide for CO_2 Photoreduction

Yunxia Zhao [1,2,3], Wei Cai [1,2,3], Jiaxin Chen [3], Yuanyuan Miao [3] and Yunfei Bu [1,2,3]*

[1] Jiangsu Collaborative Innovation Center of Atmospheric Environment and Equipment Technology, Nanjing, China, [2] Jiangsu Key Laboratory of Atmospheric Environment Monitoring and Pollution Control, Nanjing, China, [3] School of Environmental Science and Engineering, Nanjing University of Information Science and Technology, Nanjing, China

Substantial consumption of fossil fuels causes an increase in CO_2 emissions and intensifies global pollution problems, such as the greenhouse effect. Recently, a new type of ultra-low-density porous material, metal-organic frameworks (MOFs), has been developed for the photocatalytic conversion of CO_2. Herein, a composite photocatalytic catalyst based on NH_2-MIL-125(Ti) and reduced graphene oxide (rGO@NH_2-MIL-125) was fabricated through a facile "one-pot" process. The acquired materials were characterized to obtain their structures, morphologies, and optical information. The experimental results showed that methyl formate (MF) was the predominant reaction product, and rGO@NH_2-MIL-125 exhibited the highest yield of 1,116 $\mu mol \cdot g^{-1} \cdot h^{-1}$, more than twice that of pure MIL-125. The high photoactivity of rGO@NH_2-MIL-125 can be ascribed to the effective spatial separation and transfer of photoinduced carriers, largely due to the synergistic effect of amino functionality and rGO incorporation. rGO@NH_2-MIL-125 also displayed acceptable repeatability in cyclic runs for CO_2 reduction.

Keywords: CO_2 reduction, photocatalysis, metal-organic frameworks (MOFs), reduced graphene oxide, methyl formate

HIGHLIGHTS

- The agglomerate state of NH_2-MIL-125(Ti) was improved by introducing reduced graphene oxide.
- The composite catalyst could efficiently enhance photogenerated charge separation.
- The composite photocatalyst showed effective activity in reducing CO_2 in CH_3OH to $HCOOCH_3$.
- The composite catalyst exhibited acceptable stability in cyclic runs for CO_2 reduction.

INTRODUCTION

With the economic and social development, the CO_2 concentration in the atmosphere is increasing, causing global warming, and other climate problems. CO_2 emissions mainly come from mobile or immobile sources (e.g., vehicles and coal power plants). The reduction of CO_2 emissions is essential to address the global issue of climate change. Both the capture and sequestration technology of

CO_2 (Anwar et al., 2018; Luis Míguez et al., 2018) and the chemical conversion of captured CO_2 into useful chemicals or clean fuels using solar energy (Fu et al., 2018; Lee et al., 2018; Wang et al., 2018a) at normal temperatures and pressures are promising approaches that can simultaneously solve two problems by addressing global environmental pollution and energy deficiency.

Photocatalytic CO_2 reduction is one CO_2 conversion technology, and its key lies in the catalyst. In 1979, Inoue et al. (1979) synthesized semiconductor TiO_2 as a catalyst for photoirradiation of the CO_2 reduction reaction in an aqueous solution filled with CO_2. The reduction products, CH_2O, $HCOOH$, CH_3OH and CH_4, were obtained, and this result laid the foundation for photocatalytic CO_2 reduction. Thereafter, TiO_2 was continuously proven to be an efficient and promising photocatalyst (Liu G., et al., 2018; Wang et al., 2018b, 2019). Various Ti-based modified catalysts have been designed and developed for improving the CO_2 photoreduction efficiency (Jiang et al., 2018; Zhao et al., 2018). It was found that an appropriate bandgap width and band structure, good electron-hole separation performance, and abundant reaction active sites favor excellent photocatalytic efficiency (Usubharatana et al., 2006; Crake et al., 2017). Metal-organic frameworks (MOFs) are one type of porous material with ordered crystal structures constructed from metal nodes (metal ions) and organic linkers (Millward and Yaghi, 2005). In recent years, research on MOFs has spread to the catalysis and CO_2 conversion fields (Crake et al., 2017; Fang et al., 2018; Li et al., 2018a; Zhang et al., 2018). Ti-based MOFs are considered promising candidates for CO_2 photocatalytic reduction (Sun et al., 2014; Li et al., 2018a; Zhang et al., 2018) because their Ti-O clusters can be regarded as isolated titanium oxide quantum dots (Sun and Li, 2017). Fu et al. (2012) and Li et al. (2018a) studied the photocatalytic CO_2 reduction performance on MIL-125(Ti). After 10 h of UV-light irradiation, 2.41 μmol $HCOO^-$ was detected in the acetonitrile (MeCN) solvent with triethanolamine (TEOA). Then, amino-functionalized MIL-125 was also investigated for CO_2 photoreduction, and a possible mechanism for this photocatalysis reaction was proposed. After introducing the BDC linker with the amine group –NH_2, the bandgap of MIL-125 was obviously reduced (Fu et al., 2012; Xu et al., 2015), and its optical absorption performance was improved. In addition, the adsorption capability toward CO_2 was also enhanced by the amino functionality. The $HCOO^-$ yield increased to 3.83 μmol.

Even so, the NH_2-MIL-125 still has a low CO_2 reduction activity (Xu et al., 2015). To further improve the photocatalytic efficiency, graphene-like two-dimensional materials have often been incorporated into many photocatalysts via covalent or noncovalent interactions (Zhu et al., 2018). A microwave induction platform for the preparation of graphene oxide (GO)-enhanced MOF photocatalysts with highly efficient optical and electronic properties resulted in good photocatalytic oxidation performance and stability for nitric oxide and acetaldehyde (Li et al., 2018b). A strong photocatalytic hydrogen production activity up to ∼9.1-fold that of the pure MOF can be achieved by MOF@rGO because the strong π-π interactions between the MOF and rGO can

effectively accelerate the electron–hole pair separation (Karthik et al., 2018).

Herein, a NH_2-MIL-125(Ti) and reduced graphene oxide (rGO) composite was synthesized *in situ* by a facile "one-pot" method as an efficient photocatalyst for CO_2 reduction. The bare MIL-125(Ti) was also prepared to compare with NH_2-MIL-125(Ti) in order to highlight the advantage of –NH_2 based on its superior optical performance. rGO with a two-dimensional structure was expected to be a superior charge transfer medium due to its fast light transmission, outstanding conductivity and high carrier mobility (Bao and Chen, 2018). Moreover, rGO was also supposed to play a part in the structural adjustment of NH_2-MIL-125(Ti). Therefore, the objective catalyst was compared to pure MIL-125(Ti) and NH_2-MIL-125(Ti) to ascertain the synergistic effect of the –NH_2-containing linker and incorporated rGO. The photocatalytic reaction here was conducted in a catalyst-methanol slurry system at normal atmospheric pressure and temperature. MeCN, TEOA and other toxic organic solvents were avoided for use as hole scavengers. Instead, hypotoxic methanol was chosen as the reducing agent due to its high CO_2 absorption capacity.

EXPERIMENTAL

Synthesis

Pure MIL-125(Ti) was prepared through a solvothermal process referenced in the literature (Yang et al., 2017; Rahmani et al., 2018; Wang et al., 2018c). Typically, titanium isopropoxide (1.5 mmol) and H_2BDC (6 mmol) were dissolved in a mixed solvent of DMF and CH_3OH (18 mL/2 mL) under magnetic stirring for 0.5 h. Then, the solution was transferred to a Teflon-lined stainless-steel autoclave and heated at 150°C for 72 h. After being filtered, the white solid product was washed thrice with DMF and CH_3OH, respectively. During the washing process, the suspension was subjected to natural precipitation and removal of the supernatant. Finally, the MIL-125(Ti) powder was activated under vacuum drying at 80°C for 10 h.

Amino-substituted titanium MOF NH_2-MIL-125(Ti) was also prepared by a similar procedure except that H_2BDC was replaced by H_2BDC-NH_2. Finally, a yellow solid powder was obtained.

The NH_2-MIL-125(Ti) and rGO composite was synthesized according to a similar solvothermal process. First, a certain amount of GO power was dispersed into 10 mL DMF by ultrasonication for 1 h. The amount of GO added was 5 wt. % of the parent MOF. In the meantime, titanium isopropoxide (1.5 mmol) and H_2BDC (6 mmol) were dissolved in a mixed solvent of DMF and CH_3OH (18 mL/2 mL). Then, the above two were mixed together, stirred constantly for 1 h, and subjected to a solvothermal process at 150°C for 72 h. Usually, this solvothermal condition reduces GO to rGO (Yang et al., 2016a). The following procedures were the same as those for the above two pristine MOFs. The obtained gray powder was labeled as rGO@NH_2-MIL-125.

Characterization

The structures of all three obtained samples were measured by X-ray diffraction (XRD) (XD-3, Purkinjie), scanning electron

microscopy (SEM) (S4800, Hitachi) and N$_2$ absorption-desorption analysis (ASAP 2020, Micromeritics). Fourier transform infrared spectra (FT-IR) were obtained on a MB-154S infrared spectrometer (Bomen, Canada) to investigate the samples' chemical groups. The optical properties of all samples were examined by ultraviolet-visible diffuse reflectance spectroscopy (DRS) (UV-2600, Shimadzu) and photoluminescence spectroscopy (PL) (F-4500, Hitachi) with a 325 nm excitation wavelength. The photoelectrochemical measurements were performed in a CHI760 electrochemical workstation using a three-electrode electrochemical cell. A Pt wire and a Ag/AgCl electrode (3 M KCl) served as the counter and reference electrodes, respectively. The electrolyte was 0.5 M Na$_2$SO$_4$. The working electrode was FTO glass, and the sample was deposited on it by a drop casting method (Wang et al., 2018d). Five milligrams of photocatalyst powder was dispersed in 1 mL of ethanol containing 10 μL of naphthol by ultrasonication (1 h). Then, two drops of the sample solution were scattered on the FTO glass, and the coated area was fixed at 1 cm^2. After being dried at 60°C for 12 h in a vacuum oven, a homogeneous film was obtained.

Photocatalytic Activity Test

The photocatalytic activity tests of all the synthesized samples were carried out using a photochemical reaction instrument (BL-GHX-V, BiLon, China). First, pure CO$_2$ gas was bubbled into the catalyst-CH$_3$OH system (30 mg/30 mL) for saturation in a 50 mL quartz tube, which was used as the photocatalytic reactor. Then, the quartz tube was sealed, and a magnetic stirrer provided ideal mixing at the bottom. A 250 W high-pressure mercury lamp served as a light source and illuminated the photocatalytic reactor from the side. Finally, the reactant-product mixed solution was analyzed by gas chromatography (GC 9790II, Fuli, China), and the photocatalytic efficiency was assessed by the yield of the product methyl formate (MF).

RESULTS AND DISCUSSION

Catalyst Characterization

Structural Properties

The XRD patterns for the pure MOFs MIL-125, NH$_2$-MIL-125, and the composite rGO@NH$_2$-MIL-125 are presented in **Figure 1**. The strong diffraction peaks of MIL-125 at 6.8°, 9.5°, 11.6°, 16.6°, and 18.0° can be indexed to the (101), (200), (211), (222), and (312) planes, respectively (Kim et al., 2013; Wang et al., 2016; Yuan et al., 2016; Yang et al., 2017; Rahmani et al., 2018; Han et al., 2019) of its orthorhombic crystal structure. The XRD pattern of as-prepared NH$_2$-MIL-125 is in good agreement with other reports (Kim et al., 2013; Guo et al., 2015; Li et al., 2018b). The pattern also exhibits characteristic peaks similar to those of MIL-125, suggesting a similar crystal structure. The rGO@NH$_2$-MIL-125 composite possesses diffraction peaks similar to those of NH$_2$-MIL-125 but with higher intensity. This result demonstrates that NH$_2$-MIL-125 crystals were perfectly formed in the presence of rGO. Notably, no obvious typical rGO peaks (Yuan et al., 2016) are shown in the XRD pattern of the rGO@NH$_2$-MIL-125 sample due to the low amount and
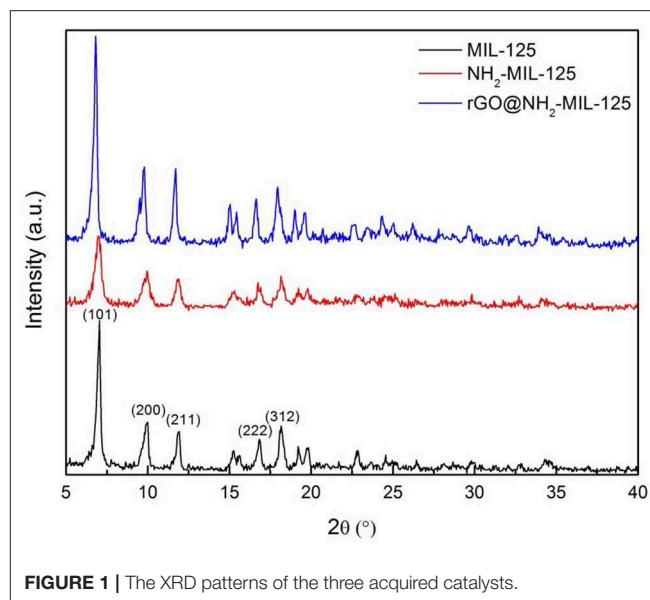

FIGURE 1 | The XRD patterns of the three acquired catalysts.

relatively low diffraction intensity of the rGO component (Yang and Xu, 2013) in comparison with the MOFs. It is interesting to discover that the diffraction peaks of rGO@NH$_2$-MIL-125 shift to the left relative to those of NH$_2$-MIL-125, which indicates strong interactions between the rGO and MOF components in the rGO@NH$_2$-MIL-125 composite. This phenomenon was also observed by Li et al. (2018b).

The morphological details of MIL-125, NH$_2$-MIL-125 and the composite rGO@NH$_2$-MIL-125 measured by SEM are shown in **Figures 2A–D**. MIL-125 has a tablet-like form and smooth surface with an average particle size of 1 μm. NH$_2$-MIL-125 exhibits a similar shape as MIL-125, but it has a much smaller size in diameter or thickness, which coincides with the results of XRD patterns. The smaller the crystal size, the wider the diffraction peak. In **Figure 2B**, it can be seen that these much smaller tablets aggregate together in piles. Obviously, the dispersion of MIL-125 particles is better than that of NH$_2$-MIL-125. From the SEM images of rGO@NH$_2$-MIL-125, it can be clearly seen that the two components are intertwined with each other. rGO has a wrinkled layered structure, and NH$_2$-MIL-125 maintains a polyhedron structure loaded on the surface of rGO. However, the shape of NH$_2$-MIL-125 particles in the composites becomes irregular due to the incorporation of rGO, as seen in the higher magnification SEM images (**Figure S1**). Compared with **Figure 2B**, the dispersion of MOF particles in **Figures 2C,D** is better, which demonstrates that aggregation could be avoided by rGO.

N$_2$ physisorption experiments were conducted to obtain the porous structures and specific surface areas of the samples. The as-prepared samples are all type I isotherms, as shown in **Figure 3A**, indicating their microporous structures, which were verified by the pore size distribution curves in **Figure 3B**. The corresponding calculated parameters are listed in **Table 1**. As shown, MIL-125, NH$_2$-MIL-125 and rGO@NH$_2$-MIL-125
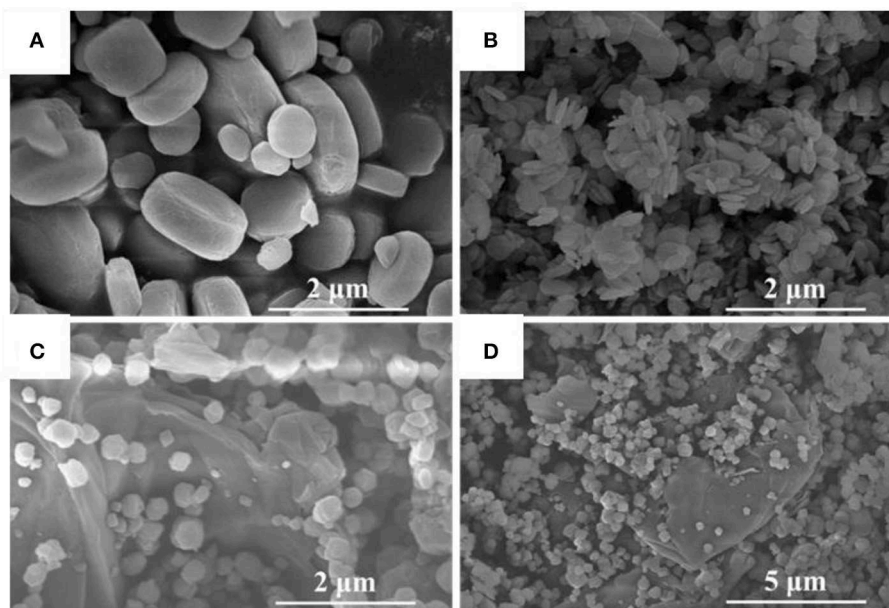
FIGURE 2 | SEM images of MIL-125 **(A)**, NH$_2$-MIL-125 **(B)**, and rGO@NH$_2$-MIL-125 **(C,D)**.
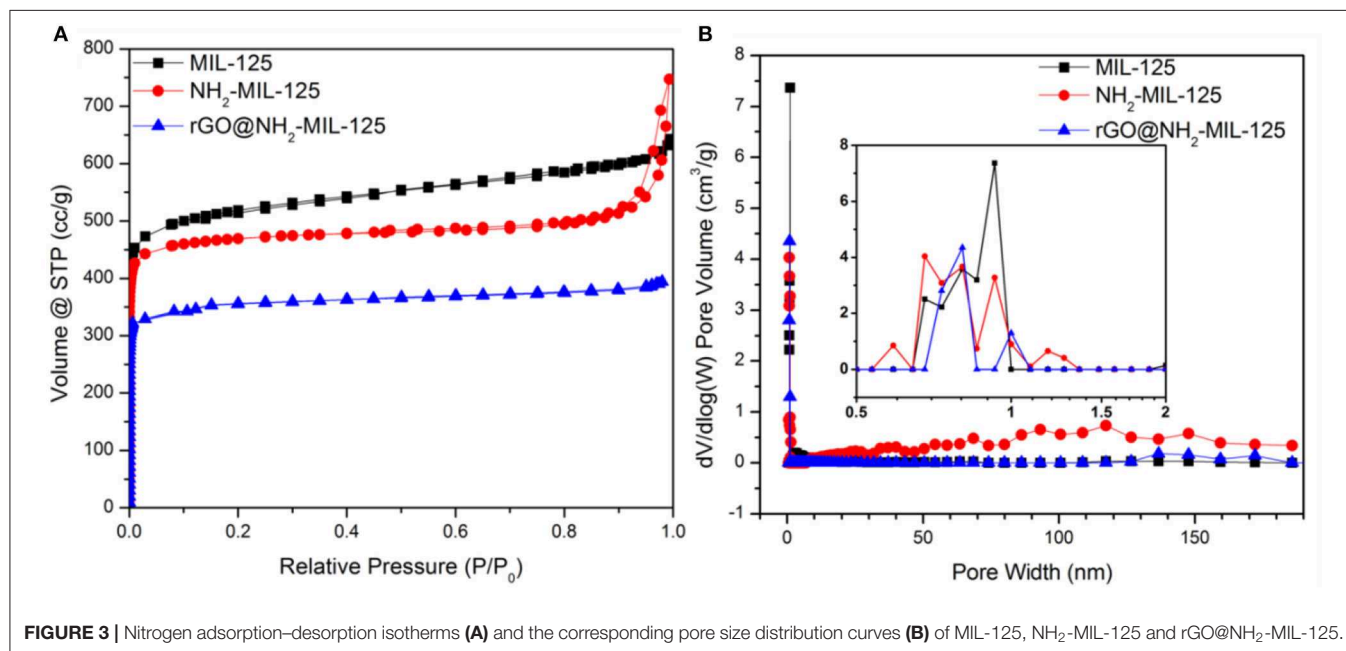

FIGURE 3 | Nitrogen adsorption–desorption isotherms **(A)** and the corresponding pore size distribution curves **(B)** of MIL-125, NH$_2$-MIL-125 and rGO@NH$_2$-MIL-125.

display Brunauer-Emmett-Telle (BET) surface areas of 1,669, 1,490, and 1,048 m^2·g^{-1}, respectively. A higher surface area can provide more active sites for photocatalytic reactions. rGO@NH$_2$-MIL-125 possesses a smaller surface area and micropore volume than NH$_2$-MIL-125. Here, the intended content of GO added in the composite was 5 wt.%. However, the surface area of the rGO@NH$_2$-MIL-125 composite obtained was much less than the value on a prorata calculation. Therefore, the introduction of rGO affected the structure

of NH$_2$-MIL-125 particle agglomerates and decreased their surface area and pore volume. As seen from the pore size distribution curves, more mesopores exist in NH$_2$-MIL-125 based on the hysteresis loop observed in its N$_2$ adsorption-desorption isotherm. This difference may be caused by its aggregated clusters, and thus, NH$_2$-MIL-125 exhibits a larger total pore volume than MIL-125 and a similar micropore ratio. When rGO is incorporated into the reaction precursor, the obtained rGO@NH$_2$-MIL-125 exhibits a lower mesopore

Samples	$S_{BET}/m^2 \cdot g^{-1}$	$V_t/cm^3 \cdot g^{-1}$	$V_{micro}/cm^3 \cdot g^{-1}$	V_{micro}/V_t
MIL-125	1,669	0.99	0.62	63%
NH₂-MIL-125	1,490	1.15	0.64	56%
rGO@NH₂-MIL-125	1,048	0.71	0.55	77%
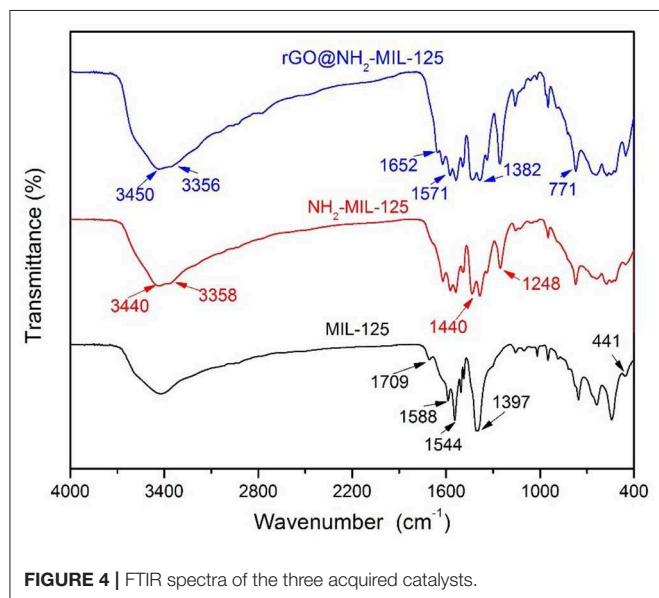
FIGURE 4 | FTIR spectra of the three acquired catalysts.

volume and a more centralized pore width distribution, which is in agreement with its higher dispersibility relative to those of NH₂-MIL-125.

Chemical Composition

Figure 4 shows the comparison of the FTIR spectra of the pure MOFs MIL-125 and NH₂-MIL-125 and the composite rGO@NH₂-MIL-125. In the FTIR spectrum of MIL-125, the large broad adsorption band in the range of 3,200~3,700 cm⁻¹ is attributed to free solvent molecules in the framework pores (Yang et al., 2017). The strong bands at 1,397~1,709 cm⁻¹ are assigned to the vibrations of carboxylate groups, which belong to the linkers in the framework of MIL-125 (Martis et al., 2013; Wang et al., 2015; Yang et al., 2017, 2018). The characteristic absorption of benzene rings is observed in the range of 800~1,200 cm⁻¹, and the O-Ti-O vibrations are located in the range of 400~800 cm⁻¹ (Yang et al., 2017, 2018). NH₂-MIL-125 possesses three similar main absorption regions as MIL-125 except the characteristic stretching vibrations of the hydroxyl at 3,440 cm⁻¹ and the amino at 3,358 cm⁻¹ (Martis et al., 2013; Wang et al., 2015; Li et al., 2018b). In addition, the strong band at 1,248 cm⁻¹ is assigned to the stretching vibrations of C-N from the aromatic amine (HadŽi and Škrbljak, 1957). rGO@NH₂-MIL-125 shows almost the same adsorption bands as NH₂-MIL-125. The absence of GO-related stretching bands for oxygen-containing functional groups confirms the effective reduction

of GO into rGO under the solvothermal reaction process. In addition, a new absorption band originating from the graphene skeletal vibration appears at 1,652 cm⁻¹, which is shifted from its common band position of 1,630 cm⁻¹ (Al Nafiey et al., 2017; Zhao et al., 2017). This shift also hints at the interactions between rGO and MOF components in the rGO@NH₂-MIL-125 composite.

Optical Properties

The optical absorption characteristics of pure MIL-125, NH₂-MIL-125 and the composite rGO@NH₂-MIL-125 were investigated by UV-vis DRS in **Figure 5A**. For MIL-125, its absorption peaks are in the UV-light range, while the pure NH₂-MIL-125 and the composite rGO@NH₂-MIL-125 absorb light from the UV to visible-light range, which can improve the utilization of solar energy and produce more electron–hole pairs. For MIL-125, the O to Ti ligand-to-metal charge transfer in TiO₅(OH) inorganic clusters was confirmed by Sun and Li (2017) and Kim et al. (2013), and H₂BDC-NH₂ or rGO apparently influences the change transfer phenomena in these TiO₅(OH) clusters in NH₂-MIL-125 or rGO@NH₂-MIL-125. Moreover, rGO@NH₂-MIL-125 possesses a higher absorption intensity than NH₂-MIL-125 at wavelengths >500 and 339~411 nm, indicating that the addition of rGO may positively affect the optical properties. In **Figure 5B**, the bandgap values can be determined from the plots of $(Ah\nu)^2$ vs. the photon energy ($h\nu$) by extrapolating the maximum slope to the x axis (Li et al., 2018b; Wu et al., 2018). For semiconducting MOFs, the bandgap is defined as the gap between the highest occupied molecular orbital (HOMO) and the lowest unoccupied molecular orbital (LUMO) according to the molecular orbital method (Maina et al., 2017; Li et al., 2018a). Thus, the HOMO-LUMO gap of MIL-125 is 3.75 eV and that for NH₂-MIL-125 is 2.69 eV, which is very close to that of the composite rGO@NH₂-MIL-125 (2.75 eV). Thus, the introduction of the amino into the BDC linker can clearly reduce the HOMO-LUMO gap value of MIL-125. The photocatalyst with a higher HOMO-LUMO gap requires light with higher energy to generate photoinduced electrons and holes. Obviously, amino groups introduced into the linkers of MIL-125 are favorable for extending the optical adsorption properties and decreasing the photodriving force.

The trapping and lifetime of photogenerated charges has a great effect on the photocatalytic activity of a semiconductor photocatalyst (Liu G., et al., 2018; Liu H., et al., 2018). The PL spectra of the three catalysts are shown in **Figure 6** since PL is usually used for evaluating the recombination of photoinduced charge carriers. The pristine MIL-125 displays a strong peak at ~525 nm. However, the PL intensities of pure NH₂-MIL-125 and the composite rGO@NH₂-MIL-125 were significantly weakened. At the optimum wavelength of 525 nm, they are very close. However, in the higher wavelength scope, the intensity of rGO@NH₂-MIL-125 is even lower. Generally, the low PL intensity can result from a low recombination rate of photogenerated electron-hole pairs (Huang et al., 2018), suggesting the longer service life of the electron hole. Thus, both the amino-functionalized linker and the rGO incorporation
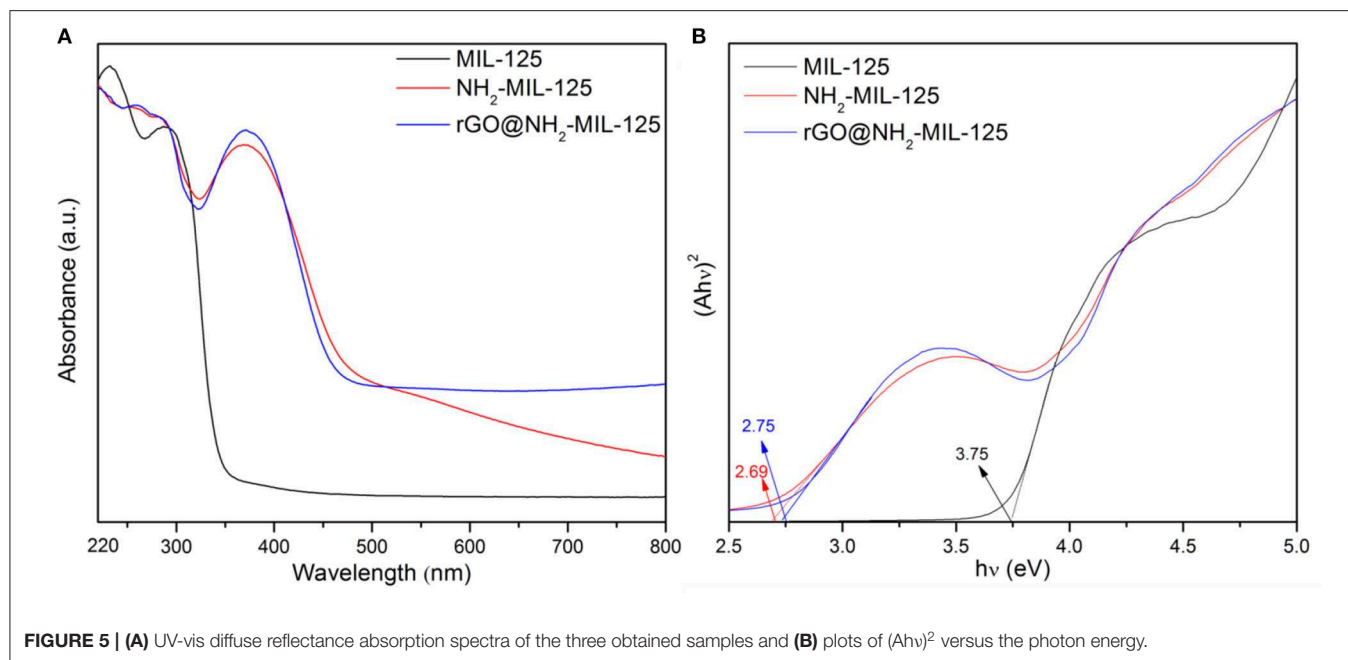
FIGURE 5 | (A) UV-vis diffuse reflectance absorption spectra of the three obtained samples and **(B)** plots of $(A h\nu)^2$ versus the photon energy.
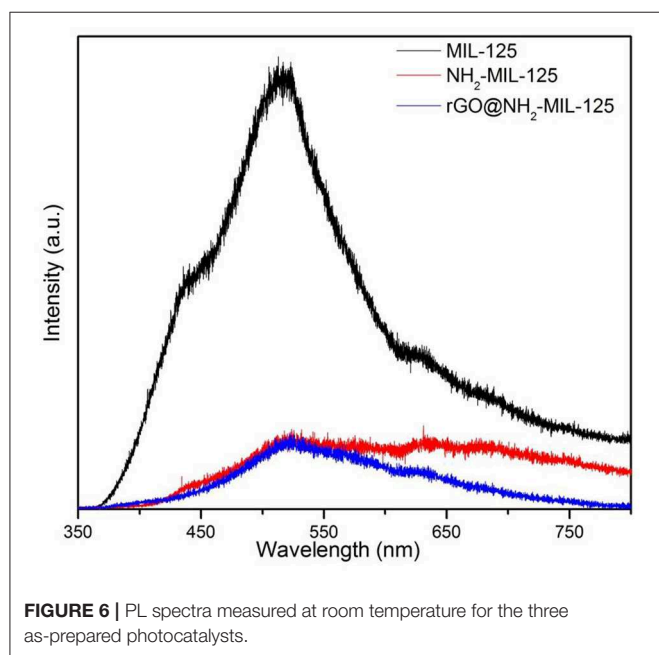

FIGURE 6 | PL spectra measured at room temperature for the three as-prepared photocatalysts.

are favorable for the mobility of photoexcited electrons and prohibiting photoinduced charge carrier recombination.

Photoelectrochemical measurements were performed to further study the charge separation and transfer efficiency of all catalysts. In **Figure 7A**, the three as-prepared samples display basically reproducible photocurrent responses during intermittent visible-light irradiation with the same time intervals. Clearly, the photocurrent densities decreased following the sequence of rGO@NH$_2$-MIL-125, NH$_2$-MIL-125, and MIL-125. A high photocurrent density is attributed to a high separation

efficiency of photogenerated electron-hole pairs (Wan et al., 2017a,b). Thus, both amino groups containing linkers and rGO benefit the efficient separation of photoinduced e$^-$ and h$^+$ for further improvement of enhancing the photocatalytic activity of MIL-125. The electrochemical impedance spectroscopy (EIS) test is another effective way to analyse the charge transfer properties. In theory, a smaller arc radius in the EIS Nyquist plot indicates a lower charge transfer resistance and represents a higher migration and transfer efficiency of photoexcited electron-hole pairs (Wan et al., 2017b; Wang et al., 2018d). In **Figure 7B**, the introduction of rGO and amino groups in MIL-125 causes a significant decrease in the arc radius, implying the lowest charge transfer resistance on the surface of the electrode with rGO@NH$_2$-MIL-125, which is consistent with the photocurrent results.

Photocatalytic CO_2 Reduction Performance

Figure 8A shows the photocatalytic activity of MIL-125, NH$_2$-MIL-125 and rGO@NH$_2$-MIL-125. These three materials were used to reduce CO_2 in CH_3OH after 4 h of light irradiation, and the predominant reaction product was MF. Since the light source was UV-light, the photon energy was enough to excite all the three photocatalysts. For the fresh samples, the data in the figure show that NH$_2$-MIL-125 has a slightly higher MF yield than MIL-125, although the former possesses a lower BET surface area. This difference might be related to the special structure and functional groups of NH$_2$-MIL-125. Excluding the surface area, the MF formation rate in units of $\mu mol \cdot m^{-2} \cdot h^{-1}$ is shown in **Figure 8B**. This result for NH$_2$-MIL-125 is superior to that of MIL-125, which is attributed to its more effective separation of photoinduced charge carriers. Among these three samples, rGO@NH$_2$-MIL-125 exhibits the highest yield of MF, which is
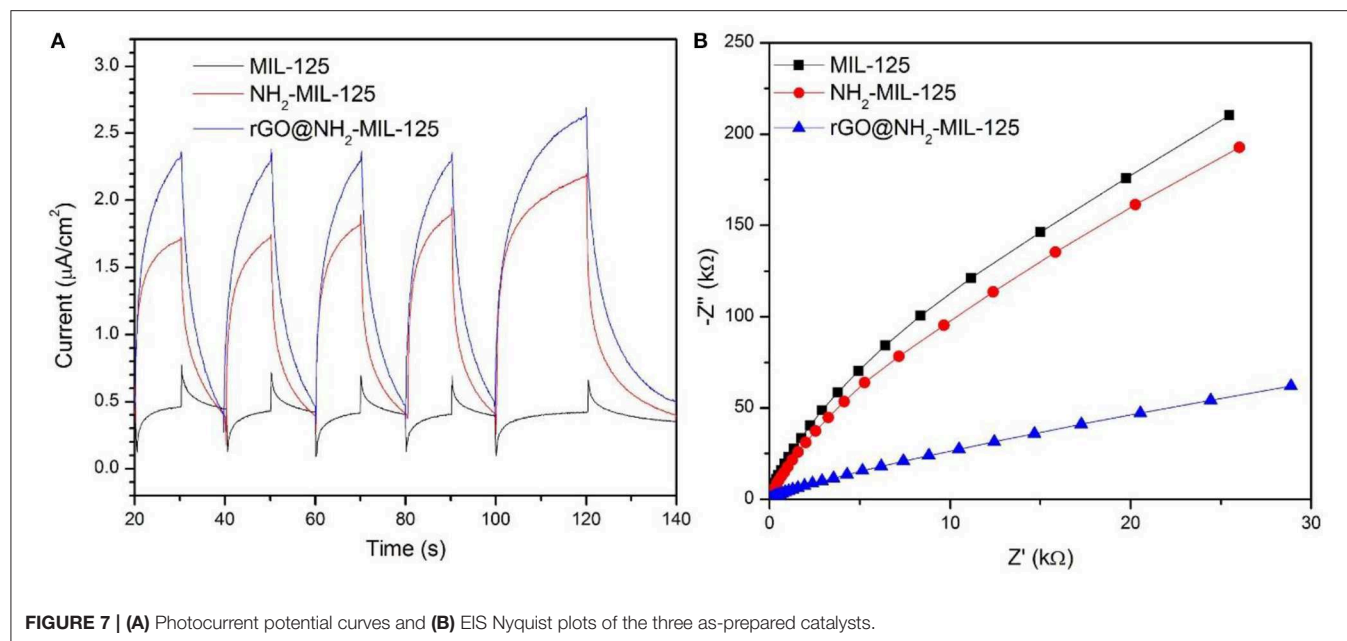
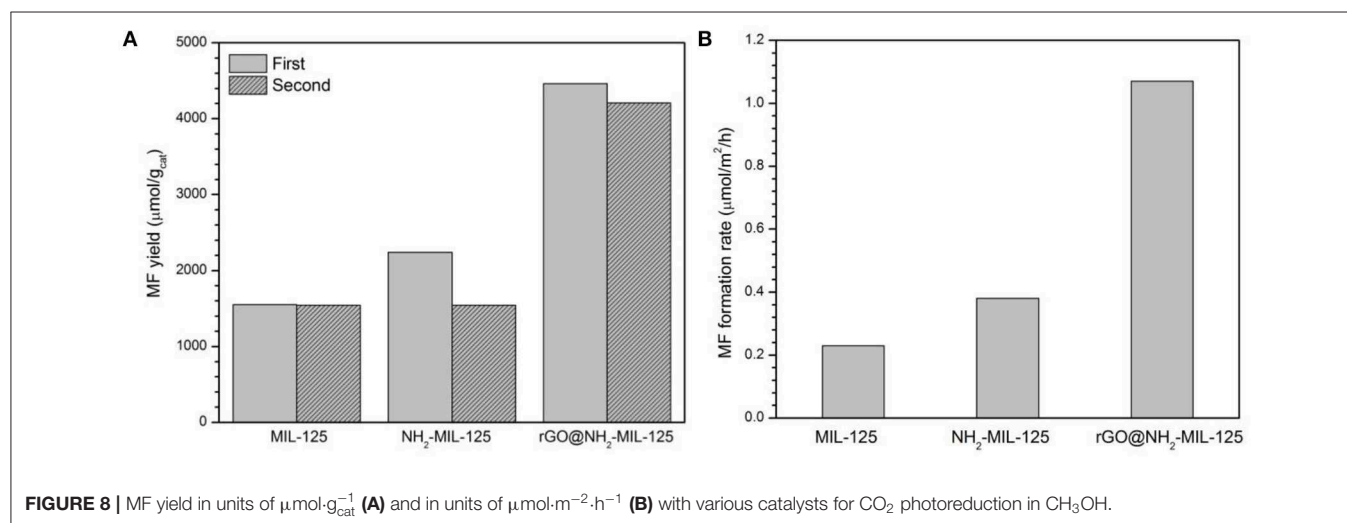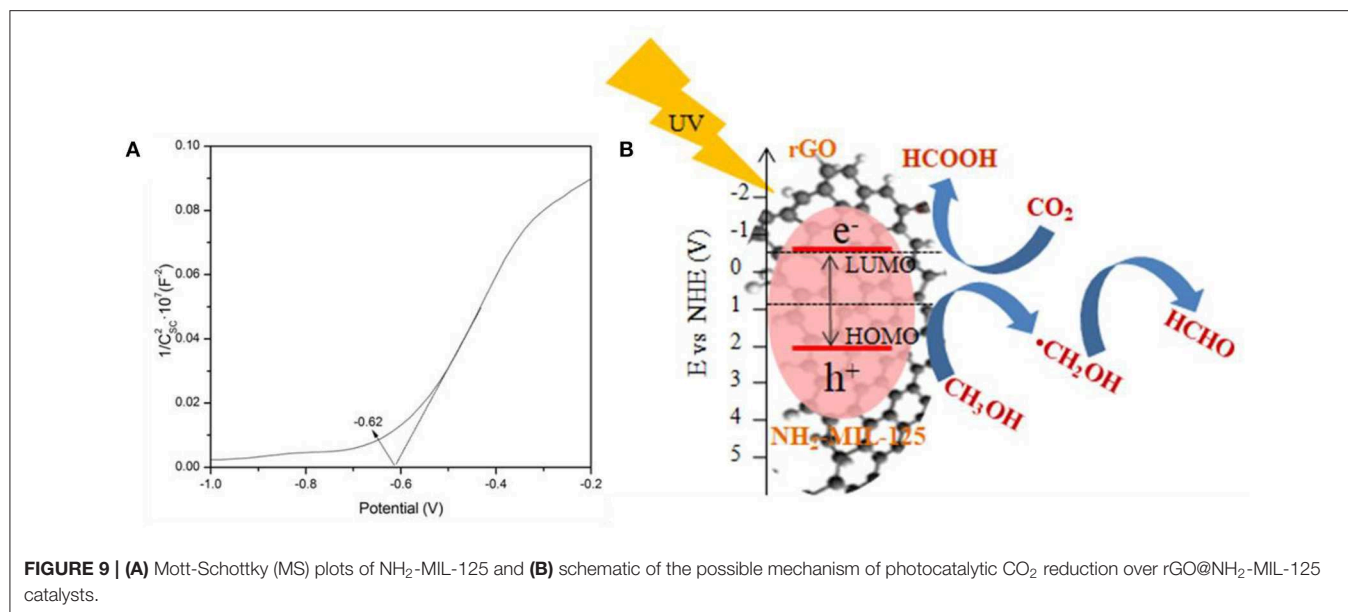**FIGURE 7 | (A)** Photocurrent potential curves and **(B)** EIS Nyquist plots of the three as-prepared catalysts.

FIGURE 8 | MF yield in units of $\mu mol \cdot g_{cat}^{-1}$ **(A)** and in units of $\mu mol \cdot m^{-2} \cdot h^{-1}$ **(B)** with various catalysts for CO_2 photoreduction in CH_3OH.

1,116 $\mu mol \cdot g^{-1} \cdot h^{-1}$ and more than twice that of pure MIL-125. This is also more than that of metal sulfides (Chen et al., 2013a,b, 2015). In addition, the honeycomb lattice of rGO allows electrons to pass rapidly. It has good electron conductivity and results in the superior catalytic performance of rGO@NH$_2$-MIL-125. Thus, the high photoactivity of rGO@NH$_2$-MIL-125 can be ascribed to the effective spatial separation and transfer of photoinduced carriers, largely due to the synergistic effect of amino functionality and rGO incorporation.

The catalysts were recovered from the photocatalytic suspension system by centrifugation after each use. In **Figure 8A**, the repeatability of the NH$_2$-MIL-125 series sample is worse than that of MIL-125, which indicates the better stability of MIL-125. According to the XRD patterns of fresh and used samples after two cycles (**Figure S2**), there is no drastic change

on their crystal structure. Only the intensities of XRD patterns of used catalysts are decreased, which can be explained by some adsorbed species in them (Sadeghi et al., 2018). The FTIR spectra of the used samples (**Figure S3**) show some new bands at 2,800~2,900 cm^{-1} and 3,500~3,600 cm^{-1} from CH_3OH (Forester and Howe, 1987), indicating that the adsorbed specie was methanol in the recycled catalysts. To further investigate the recyclability of rGO@NH$_2$-MIL-125 with the best photocatalysis activity, four times cycling tests of photocatalytic CO_2 reduction over it were conducted. As shown in **Figure S4**, the yields of MF are still above 85% after four cycles, which indicates acceptable recyclability of GO@NH$_2$-MIL-125 for photocatalytic CO_2 reduction. In the future, the stability of the photocatalysts in cyclic runs is expected to improve by optimizing the recycling operations.

FIGURE 9 | (A) Mott-Schottky (MS) plots of NH_2-MIL-125 and **(B)** schematic of the possible mechanism of photocatalytic CO_2 reduction over rGO@NH_2-MIL-125 catalysts.

To clarify the possible mechanism for the photocatalytic CO_2 reduction in CH_3OH solution over rGO@NH_2-MIL-125 catalysts under UV-light irradiation, the band structure of NH_2-MIL-125 was investigated by Mott–Schottky measurements, and the Mott-Schottky plot is shown in **Figure 9A**. The positive slope of the plot indicates that NH_2-MIL-125 is an n-type semiconductor (Yang et al., 2016a). If NH_2-MIL-125 is set as a conventional semiconductor, the X-axis intercept of −0.62 of the linear region can be considered its flat band potential (V_{fb}) with the unit V vs. Ag/AgCl. According to the equation (Ao et al., 2018; Cai et al., 2018; Wang et al., 2018d), E (NHE, normal hydrogen electrode) $= E(Ag/AgCl) + 0.1976$ V, the converted potential NHE is obtained. Since V_{fb} is generally 0.2 V more positive than the conduction band (CB) potential (E_{CB}) for an n-type semiconductor (Chen et al., 2013a; Wang et al., 2018d), the calculated E_{CB} is ∼-0.62 V vs. NHE. Based on the corresponding LUMO potential of NH_2-MIL-125 (−0.62 V) (Zhao et al., 2019) and the bandgap (HOMO–LUMO gap width) in **Figure 5A**, the position of the HOMO energy level is further estimated to be 2.07 V vs. NHE. Under UV-light irradiation, NH_2-MIL-125 can absorb photon energy and then be excited to generate electron-hole pairs. The electrons in the LUMO of NH_2-MIL-125 transfer to the rGO surface due to its excellent electron mobility (Li et al., 2018c; Zhu et al., 2018), while the holes can remain on the HOMO of NH_2-MIL-125 since the recombination of photogenerated charge carriers is greatly inhibited. As reported by Wan et al. (2017a), rGO itself doesn't contribute to the generation of electrons and holes under light irradiation. It only serves as an electron conductor medium. Thus, the introduction of rGO offers a greater range of carrier motion, which can efficiently suppress the recombination of photoinduced electrons and holes as well as increase the ability of electronic transmission. A possible mechanism is proposed, as displayed in **Figure 9B**, according to the above HOMO–LUMO structure. The HOMO of NH_2-MIL-125 is more positive than

the reported $E_0(CH_3OH/\cdot CH_2OH)$ (0.927 V) (Qin et al., 2011; Yang et al., 2016b; Chen et al., 2017; Ao et al., 2018), so the photoinduced holes can oxidize CH_3OH into HCHO with H^+ formation. The LUMO of NH_2-MIL-125 is negative than $E_0(CO_2/HCOOH)$ (−0.61 V) (Qin et al., 2011; Yang et al., 2016b; Chen et al., 2017; Ao et al., 2018) and can reduce CO_2 into HCOOH in the presence of H^+. Finally, MF can be produced not only via the esterification of HCOOH and CH_3OH but also by the dimerization of HCHO based on the Tishchenko reaction (Qin et al., 2011; Yang et al., 2016b; Chen et al., 2017).

CONCLUSIONS

The composite rGO@NH_2-MIL-125 was fabricated *in situ* through a "one-pot" solvothermal process. The agglomerated state of NH_2-MIL-125(Ti) was improved by introducing rGO. Its photocatalytic activity was evaluated by the photocatalytic CO_2 reduction in CH_3OH solution and compared with those of the other two prepared samples MIL-125 and NH_2-MIL-125. The results showed that MF was the predominant reaction product, and rGO@NH_2-MIL-125 exhibited the highest yield of 1,116 $\mu mol \cdot g^{-1} \cdot h^{-1}$, which is two times more than that of pure MIL-125. The effective separation of photogenerated electrons and holes largely due to the synergistic effect of amino functionality and rGO incorporation contributed to the high photoactivity of rGO@NH_2-MIL-125. It also displayed acceptable repeatability in cyclic runs for CO_2 photocatalytic reduction. However, its repeatability without achieving the largest value indicates that optimization of the recovery processes in future research can further improve the stability of the photocatalysts in cyclic runs.

DATA AVAILABILITY STATEMENT

The datasets generated for this study are available on request to the corresponding author.

AUTHOR CONTRIBUTIONS

FUNDING

SUPPLEMENTARY MATERIAL

REFERENCES

Al Nafiey, A., Addad, A., Sieber, B., Chastanet, G., Barras, A., Szunerits, S., et al. (2017). Reduced graphene oxide decorated with Co₃O₄ nanoparticles (rGO-Co₃O₄) nanocomposite: a reusable catalyst for highly efficient reduction of 4-nitrophenol, and Cr(VI) and dye removal from aqueous solutions. *Chem. Eng. J.* 322, 375–384. doi: 10.1016/j.cej.2017.04.039

Anwar, M. N., Fayyaz, A., Sohail, N. F., Khokhar, M. F., Baqar, M., Khan, W. D., et al. (2018). CO₂ capture and storage: a way forward for sustainable environment. *J. Environ. Manage.* 226, 131–144. doi: 10.1016/j.jenvman.2018.08.009

Ao, D., Zhang, J., and Liu, H. (2018). Visible-light-driven photocatalytic degradation of pollutants over Cu-doped NH₂-MIL-125 (Ti). *J. Photoch. Photobi.* 364, 524–533. doi: 10.1016/j.jphotochem.2018.06.044

Bao, Y., and Chen, K. (2018). Novel Z-scheme BiOBr/reduced graphene oxide/protonated g-C₃N₄ photocatalyst: synthesis, characterization, visible light photocatalytic activity and mechanism. *Appl. Surf. Sci.* 437, 51–61. doi: 10.1016/j.apsusc.2017.12.075

Cai, W., Shi, Y., Zhao, Y., Chen, M., Zhong, Q., and Bu, Y. (2018). The solvent-driven formation of multi-morphological Ag-CeO₂ plasmonic photocatalysts with enhanced visible-light photocatalytic reduction of CO₂. *RSC Adv.* 8, 40731–40739. doi: 10.1039/C8RA08938H

Chen, J., Qin, S., Song, G., Xiang, T., Xin, F., and Yin, X. (2013b). Shape-controlled solvothermal synthesis of Bi₂S₃ for photocatalytic reduction of CO₂ to methyl formate in methanol. *Dalton T.* 42, 15133–15138. doi: 10.1039/c3dt51887f

Chen, J., Xin, F., Niu, H., Mao, C.-J., and Song, J.-M. (2017). Photocatalytic reduction of CO₂ with methanol over Bi₂S₃-ZnIn₂S₄ nanocomposites. *Mater. Lett.* 198, 1–3. doi: 10.1016/j.matlet.2017.03.164

Chen, J., Xin, F., Qin, S., and Yin, X. (2013a). Photocatalytically reducing CO₂ to methyl formate in methanol over ZnS and Ni-doped ZnS photocatalysts. *Chem. Eng. J.* 230, 506–512. doi: 10.1016/j.cej.2013.06.119

Chen, J., Xin, F., Yin, X., Xiang, T., and Wang, Y. (2015). Synthesis of hexagonal and cubic ZnIn₂S₄ nanosheets for the photocatalytic reduction of CO₂ with methanol. *RSC Adv.* 5, 3833–3839. doi: 10.1039/C4RA13191F

Crake, A., Christoforidis, K. C., Kafizas, A., Zafeiratos, S., and Petit, C. (2017). CO₂ capture and photocatalytic reduction using bifunctional TiO₂/MOF nanocomposites under UV–vis irradiation. *Appl. Catal. B* 210, 131–140. doi: 10.1016/j.apcatb.2017.03.039

Fang, Y., Ma, Y., Zheng, M., Yang, P., Asiri, A. M., and Wang, X. (2018). Metal–organic frameworks for solar energy conversion by photoredox catalysis. *Coordin. Chem. Rev.* 373, 83–115. doi: 10.1016/j.ccr.2017.09.013

Forester, T. R., and Howe, R. F. (1987). In situ FTIR studies of methanol and dimethyl ether in ZSM-5. *J. Am. Chem. Soc.* 109, 5076–5082. doi: 10.1021/ja00251a004

Fu, Y., Sun, D., Chen, Y., Huang, R., Ding, Z., Fu, X., et al. (2012). An amine-functionalized titanium metal-organic framework photocatalyst with visible-light-induced activity for CO₂ reduction. *Angew. Chem. Int. Edit.* 51, 3364–3367. doi: 10.1002/anie.201108357

Fu, Y., Zhu, X., Huang, L., Zhang, X., Zhang, F., and Zhu, W. (2018). Azine-based covalent organic frameworks as metal-free visible light photocatalysts for CO₂ reduction with H₂O. *Appl. Catal. B* 239, 46–51. doi: 10.1016/j.apcatb.2018.08.004

Guo, X., Huang, H., Ban, Y., Yang, Q., Xiao, Y., Li, Y., et al. (2015). Mixed matrix membranes incorporated with amine-functionalized titanium-based metal-organic framework for CO₂/CH₄ separation. *J. Membrane Sci.* 478, 130–139. doi: 10.1016/j.memsci.2015.01.007

HadŽi, D., and Škrbljak, M. (1957). Infrared absorption bands associated with the NH group. Part I. Some secondary aromatic amines. *J. Chem. Soc.* 158, 843–847. doi: 10.1039/JR9570000843

Han, X., Yang, X., Liu, G., Li, Z., and Shao, L. (2019). Boosting visible light photocatalytic activity via impregnation-induced RhB-sensitized MIL-125(Ti). *Chem. Eng. Res. Des.* 143, 90–99. doi: 10.1016/j.cherd.2019.01.010

Huang, Z., Chen, H., Zhao, L., He, X., Li, W., Fang, W., et al. (2018). Biogenic hierarchical MIL-125/TiO₂@SiO₂ derived from rice husk and enhanced photocatalytic properties for dye degradation. *Photochem. Photobiol.* 94, 512–520. doi: 10.1111/php.12873

Inoue, T., Fujishima, A., Konishi, S., and Honda, K. (1979). Photoelectrocatalytic reduction of carbon dioxide in aqueous suspensions of semiconductor powders. *Nature* 277, 637–638. doi: 10.1038/277637a0

Jiang, Z., Zhang, X., Yuan, Z., Chen, J., Huang, B., Dionysiou, D. D., et al. (2018). Enhanced photocatalytic CO₂ reduction via the synergistic effect between Ag and activated carbon in TiO₂/AC-Ag ternary composite. *Chem. Eng. J.* 348, 592–598. doi: 10.1016/j.cej.2018.04.180

Karthik, P., Vinoth, R., Zhang, P., Choi, W., Balaraman, E., and Neppolian, B. (2018). π-π interaction between metal–organic framework and reduced graphene oxide for visible-light photocatalytic H₂ production. *ACS Appl. Energ. Mater.* 1, 1913–1923. doi: 10.1021/acsaem.7b00245

Kim, S. N., Kim, J., Kim, H. Y., Cho, H. Y., and Ahn, W. S. (2013). Adsorption/catalytic properties of MIL-125 and NH₂-MIL-125. *Catal. Today* 204, 85–93. doi: 10.1016/j.cattod.2012.08.014

Lee, Y. Y., Jung, H. S., Kim, J. M., and Kang, Y. T. (2018). Photocatalytic CO₂ conversion on highly ordered mesoporous materials: comparisons of metal oxides and compound semiconductors. *Appl. Catal. B* 224, 594–601. doi: 10.1016/j.apcatb.2017.10.068

Li, R., Zhang, W., and Zhou, K. (2018a). Metal-organic-framework-based catalysts for photoreduction of CO₂. *Adv. Mater.* 30, 1705512–1705542. doi: 10.1002/adma.201705512

Li, S., Zhu, T., Dong, L., and Dong, M. (2018c). Boosted visible light photodegradation activity of boron doped rGO/g-C₃N₄ nanocomposites: the role of C-O-C bonds. *N. J. Chem.* 42, 17644–17651. doi: 10.1039/C8NJ03571G

Li, X., Le, Z., Chen, X., Li, Z., Wang, W., Liu, X., et al. (2018b). Graphene oxide enhanced amine-functionalized titanium metal organic framework for visible-light-driven photocatalytic oxidation of gaseous pollutants. *Appl. Catal. B* 236, 501–508. doi: 10.1016/j.apcatb.2018.05.052

Liu, G., Wang, G., Hu, Z., Su, Y., and Zhao, L. (2018). Ag₂O nanoparticles decorated TiO₂ nanofibers as a p-n heterojunction for enhanced photocatalytic decomposition of RhB under visible light irradiation. *Appl. Surf. Sci.* 465, 902–910. doi: 10.1016/j.apsusc.2018.09.216

Liu, H., Zhang, J., and Ao, D. (2018). Construction of heterostructured ZnIn₂S₄@NH₂-MIL-125(Ti) nanocomposites for visible-light-driven H₂ production. *Appl. Catal. B* 221, 433–442. doi: 10.1016/j.apcatb.2017.09.043

Luis Míguez, J., Porteiro, J., Pérez-Orozco, R., Patiño, D., and Rodríguez, S. (2018). Evolution of CO$_2$ capture technology between 2007 and 2017 through the study of patent activity. *Appl. Energ.* 211, 1282–1296. doi: 10.1016/j.apenergy.2017.11.107

Maina, J. W., Pozo-Gonzalo, C., Kong, L., Schütz, J., Hill, M., and Dumée, L. F. (2017). Metal organic framework based catalysts for CO$_2$ conversion. *Mater. Horiz.* 4, 345–361. doi: 10.1039/C6MH00484A

Martis, M., Mori, K., Fujiwara, K., Ahn, W.-S., and Yamashita, H. (2013). Amine-functionalized MIL-125 with imbedded palladium nanoparticles as an efficient catalyst for dehydrogenation of formic acid at ambient temperature. *J. Phys. Chem.* 117, 22805–22810. doi: 10.1021/jp4069027

Millward, A. R., and Yaghi, O. M. (2005). Metal-organic frameworks with exceptionally high capacity for storage of carbon dioxide at room temperature. *J. Am. Chem. Soc.* 127, 17998–17999. doi: 10.1021/ja0570032

Qin, S., Xin, F., Liu, Y., Yin, X., and Ma, W. (2011). Photocatalytic reduction of CO$_2$ in methanol to methyl formate over CuO-TiO$_2$ composite catalysts. *J. Colloid Interface Sci.* 356, 257–261. doi: 10.1016/j.jcis.2010.12.034

Rahmani, A., Emrooz, H. B. M., Abedi, S., and Morsali, A. (2018). Synthesis and characterization of CdS/MIL-125 (Ti) as a photocatalyst for water splitting. *Mat. Sci. Semicon. Proc.* 80, 44–51. doi: 10.1016/j.mssp.2018.02.013

Sadeghi, N., Sharifnia, S., and Do, T.-O. (2018). Enhanced CO$_2$ photoreduction by graphene-porphyrin metal-organic framework under visible light irradiation. *J. Mater. Chem.* 6, 18031–18035. doi: 10.1039/C8TA07158F

Sun, D., and Li, Z. (2017). Robust Ti- and Zr-based metal-organic frameworks for photocatalysis. *Chin. J. Chem.* 35, 135–147. doi: 10.1002/cjoc.201600647

Sun, D., Liu, W., Fu, Y., Fang, Z., Sun, F., Fu, X., et al. (2014). Noble metals can have different effects on photocatalysis over metal-organic frameworks (MOFs): a case study on M/NH$_2$-MIL-125(Ti) (M=Pt and Au). *Chem. Eur. J.* 20, 4780–4788. doi: 10.1002/chem.201304067

Usubharatana, P., McMartin, D., Veawab, A., and Tontiwachwuthikul, P. (2006). Photocatalytic process for CO$_2$ emission reduction from industrial flue gas streams. *Ind. Eng. Chem. Res.* 45, 2558–2568. doi: 10.1021/ie0505763

Wan, S., Ou, M., Zhong, Q., Zhang, S., and Cai, W. (2017b). Supramolecular synthesis of multifunctional holey carbon nitride nanosheet with high-efficiency photocatalytic performance. *Adv. Optical Mater.* 5:1700536. doi: 10.1002/adom.201700536

Wan, S., Ou, M., Zhong, Q., Zhang, S., and Song, F. (2017a). Construction of Z-scheme photocatalytic systems using ZnIn$_2$S$_4$, CoO$_x$-loaded Bi$_2$MoO$_6$ and reduced graphene oxide electron mediator and its efficient nonsacrificial water splitting under visible light. *Chem. Eng. J.* 325, 690–699. doi: 10.1016/j.cej.2017.05.047

Wang, H., Yuan, X., Wu, Y., Zeng, G., Chen, X., Leng, L., et al. (2015). Facile synthesis of amino-functionalized titanium metal-organic frameworks and their superior visible-light photocatalytic activity for Cr(VI) reduction. *J. Hazard. Mater.* 286, 187–194. doi: 10.1016/j.jhazmat.2014.11.039

Wang, H., Yuan, X., Wu, Y., Zeng, G., Dong, H., Chen, X., et al. (2016). In situ synthesis of In$_2$S$_3$@MIL-125(Ti) core-shell microparticle for the removal of tetracycline from wastewater by integrated adsorption and visible-light-driven photocatalysis. *Appl. Catal. B* 186, 19–29. doi: 10.1016/j.apcatb.2015.12.041

Wang, J., Wang, G., Wang, X., Wu, Y., Su, Y., and Tang, H. (2019). 3D/2D direct Z-scheme heterojunctions of hierarchical TiO$_2$ microflowers/g-C$_3$N$_4$ nanosheets with enhanced charge carrier separation for photocatalytic H$_2$ evolution. *Carbon* 149, 618–626. doi: 10.1016/j.carbon.2019.04.088

Wang, J., Wang, G., Wei, X., Liu, G., and Li, J. (2018b). ZnO nanoparticles implanted in TiO$_2$ macrochannels as an effective direct Z-scheme heterojunction photocatalyst for degradation of RhB. *Appl. Surf. Sci.* 456, 666–675. doi: 10.1016/j.apsusc.2018.06.182

Wang, Q., Wang, G., Liang, X., Dong, X., and Zhang, X. (2018c). Supporting carbon quantum dots on NH$_2$-MIL-125 for enhanced photocatalytic degradation of organic pollutants under a broad spectrum irradiation. *Appl. Surf. Sci.* 467, 320–327. doi: 10.1016/j.apsusc.2018.05.082

Wang, S., Guan, B. Y., and Lou, X. W. D. (2018a). Construction of ZnIn$_2$S$_4$-In$_2$O$_3$ hierarchical tubular heterostructures for efficient CO$_2$ photoreduction. *J. Am. Chem. Soc.* 140, 5037–5040. doi: 10.1021/jacs.8b02200

Wang, Y., Zeng, Y., Wan, S., Cai, W., Song, J., Zhang, S., et al. (2018d). *In situ* fabrication of 3D octahedral g-C$_3$N$_4$/BiFeWO$_x$ double-heterojunction for

highly selective CO$_2$ photoreduction to CO under visible light. *ChemCatChem* 10, 4578–4585. doi: 10.1002/cctc.201800959

Wu, Z., Huang, X., Zheng, H., Wang, P., Hai, G., Dong, W., et al. (2018). Aromatic heterocycle-grafted NH$_2$-MIL-125(Ti) via conjugated linker with enhanced photocatalytic activity for selective oxidation of alcohols under visible light. *Appl. Catal. B* 224, 479–487. doi: 10.1016/j.apcatb.2017.10.034

Xu, H.-Q., Hu, J., Wang, D., Li, Z., Zhang, Q., Luo, Y., et al. (2015). Visible-light photoreduction of CO$_2$ in a metal–organic framework: boosting electron–hole separation via electron trap states. *J. Am. Chem. Soc.* 137, 13440–13443. doi: 10.1021/jacs.5b08773

Yang, M.-Q., and Xu, Y.-J. (2013). Basic principles for observing the photosensitizer role of graphene in the graphene–semiconductor composite photocatalyst from a case study on graphene–ZnO. *J. Phys. Chem.* 117, 21724–21734. doi: 10.1021/jp408400c

Yang, X., Xin, W., Yin, X., and Shao, X. (2016b). Enhancement of photocatalytic activity in reducing CO$_2$ over CdS/g-C$_3$N$_4$ composite catalysts under UV light irradiation. *Chem. Phys. Lett.* 651, 127–132. doi: 10.1016/j.cplett.2016.03.027

Yang, Z., Ding, J., Feng, J., He, C., Li, Y., Tong, X., et al. (2018). Preparation of BiVO$_4$/MIL-125(Ti) composite with enhanced visible-light photocatalytic activity for dye degradation. *Appl. Organometal. Chem.* 32:e4285. doi: 10.1002/aoc.4285

Yang, Z., Xu, X., Liang, X., Lei, C., Cui, Y., Wu, W., et al. (2017). Construction of heterostructured MIL-125/Ag/g-C$_3$N$_4$ nanocomposite as an efficient bifunctional visible light photocatalyst for the organic oxidation and reduction reactions. *Appl. Catal. B* 205, 42–54. doi: 10.1016/j.apcatb.2016.12.012

Yang, Z., Xu, X., Liang, X., Lei, C., Wei, Y., He, P., et al. (2016a). MIL-53(Fe)-graphene nanocomposites: Efficient visible-light photocatalysts for the selective oxidation of alcohols. *Appl. Catal. B* 198, 112–123. doi: 10.1016/j.apcatb.2016.05.041

Yuan, X., Wang, H., Wu, Y., Zeng, G., Chen, X., Leng, L., et al. (2016). One-pot self-assembly and photoreduction synthesis of silver nanoparticle-decorated reduced graphene oxide/MIL-125(Ti) photocatalyst with improved visible light photocatalytic activity. *Appl. Organomet. Chem.* 30, 289–296. doi: 10.1002/aoc.3430

Zhang, H., Li, J., Tan, Q., Lu, L., Wang, Z., and Wu, G. (2018). Metal-organic frameworks and their derived materials as electrocatalysts and photocatalysts for CO$_2$ reduction: progress, challenge, and perspective. *Chem. Eur. J.* 24, 18137–18157. doi: 10.1002/chem.201803083

Zhao, Y., Chen, J., Cai, W., Bu, Y., Huang, Q., Tao, T., et al. (2019). CuO-decorated dual-phase TiO$_2$ microspheres with enhanced activity for photocatalytic CO$_2$ reduction in liquid–solid regime. *Chem. Phys. Lett.* 725, 66–74. doi: 10.1016/j.cplett.2019.04.010

Zhao, Y., Liu, L., Cui, T., Tong, G., and Wu, W. (2017). Enhanced photocatalytic properties of ZnO/reduced graphene oxide sheets (rGO) composites with controllable morphology and composition. *Appl. Surf. Sci.* 412, 58–68. doi: 10.1016/j.apsusc.2017.03.207

Zhao, Y., Wei, Y., Wu, X., Zheng, H., Zhao, Z., Liu, J., et al. (2018). Graphene-wrapped Pt/TiO$_2$ photocatalysts with enhanced photogenerated charges separation and reactant adsorption for high selective photoreduction of CO$_2$ to CH$_4$. *Appl. Catal. B* 226, 360–372. doi: 10.1016/j.apcatb.2017.12.071

Zhu, K., Luo, Q., Kang, S.-Z., Qin, L., Li, G.-D., and Li, X. (2018). The study of a novel cobalt implanted pyridylporphyrin/graphene oxide nanohybrid for enhanced photocatalytic hydrogen evolution and its electron transfer mechanism. *Nanoscale* 10, 18635–18641. doi: 10.1039/C8NR06138F